JACS
JOURNAL OF THE AMERICAN CHEMICAL SOCIETY
Article
pubs.acs.org/JACS

Color Theorems, Chiral Domain Topology, and Magnetic Properties of Fe_xTaS_2

Yoichi Horibe,[†,¶] Junjie Yang,[‡,§] Yong-Heum Cho,[‡,§] Xuan Luo,[‡,§] Sung Baek Kim,[‡,§,△] Yoon Seok Oh,[†] Fei-Ting Huang,[†] Toshihiro Asada,[∥] Makoto Tanimura,[∥] Dalyoung Jeong,[⊥] and Sang-Wook Cheong*[,†,‡]

[†]Rutgers Center for Emergent Materials and Department of Physics & Astronomy, Rutgers University, Piscataway, New Jersey 08854, United States

[‡]Laboratory for Pohang Emergent Materials, Pohang University of Science and Technology, Pohang 790-784, Korea

[§]Department of Physics, Pohang University of Science and Technology, Pohang 790-784, Korea

[∥]Research Department, Nissan Arc, Ltd., Yokosuka, Kanagawa 237-0061, Japan

[⊥]Department of Mathematics, Soongsil University, Seoul 156-743, Korea

Supporting Information

ABSTRACT: Common mathematical theories can have profound applications in understanding real materials. The intrinsic connection between aperiodic orders observed in the Fibonacci sequence, Penrose tiling, and quasicrystals is a well-known example. Another example is the self-similarity in fractals and dendrites. From transmission electron microscopy experiments, we found that Fe_xTaS_2 crystals with $x = 1/4$ and $1/3$ exhibit complicated antiphase and chiral domain structures related to ordering of intercalated Fe ions with 2a × 2a and $\sqrt{3}$a × $\sqrt{3}$a superstructures, respectively. These complex domain patterns are found to be deeply related with the four color theorem, stating that four colors are sufficient to identify the countries on a planar map with proper coloring and its variations for two-step proper coloring. Furthermore, the domain topology is closely relevant to their magnetic properties. Our discovery unveils the importance of understanding the global topology of domain configurations in functional materials.

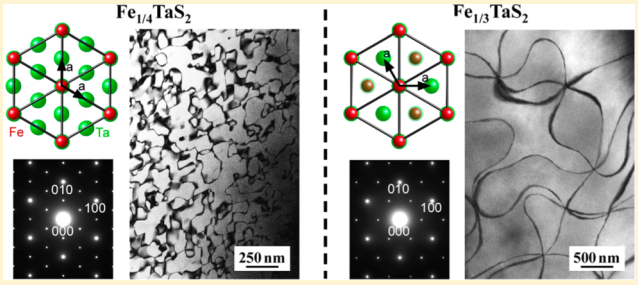

INTRODUCTION

Understanding and controlling domains and domain walls is quintessential for identifying the origin of the macroscopic physical properties of functional materials and exploiting them for technological applications. Domains are associated with different orientations of directional order parameters such as magnetization, polarization, and ferroelastic distortions.[1−3] Even though the local conditions at, for example, ferroelastic boundaries and liquid crystal defects have been often studied,[4,5] research on the macroscopic topological constraints in complex domain patterns has been scarce.

Layered transition metal dichalcogenides, consisting of MC_2 layers (M: transition metal elements, C: chalcogen elements), exhibit fascinating physical properties such as charge density waves (CDWs),[6] superconductivity,[6−9] and discommensurations.[10−15] Intercalation of other transition metal ions between the MC_2 layers gives rise to distinct superstructures, leading to significant changes in crystallographic structures and physical properties. Fe-intercalated TaS_2 shows highly anisotropic ferromagnetism at low temperatures.[16−20] Ordering of the intercalated Fe ions in Fe_xTaS_2 with $x = 1/4$ and $1/3$ results in 2a × 2a and $\sqrt{3}$a × $\sqrt{3}$a superstructures (a: the hexagonal lattice parameter of nonintercalated TaS_2) with the space groups of centrosymmetric $P6_3/mmc$ and noncentrosymmetric (chiral) $P6_322$, respectively.[16,17] These 2a × 2a and $\sqrt{3}$a × $\sqrt{3}$a superstructures are accompanied by four types (A, B, C, and D) and three types (A, B, and C) of structural antiphase domains in each intercalated Fe plane of $Fe_{1/4}TaS_2$ and $Fe_{1/3}TaS_2$, respectively. These antiphase domains are associated with the different origins (i.e., phase shifts) of the superstructures.

Herein, we report that the global topology of the antiphase and chiral domain patterns in Fe_xTaS_2 appears to be complex but can be neatly understood in terms of the four color theorem[21−23] as well as a tensorial color theorem associated with two-step proper coloring. The four color theorem, which was empirically known to cartographers before the 17th century, states that four colors are sufficient to identify the countries on a planar map with proper coloring (without bordering countries sharing the same color, except for intersections). The tensorial coloring is found to be related to the presence of chiral and antiphase domains in $Fe_{1/3}TaS_2$. Intriguingly, the global domain patterns associated with color theorems are directly relevant to bulk magnetic properties in Fe_xTaS_2. The relevance of color theorems to the domain

Received: March 14, 2014
Published: May 19, 2014

dx.doi.org/10.1021/ja5026134 | J. Am. Chem. Soc. 2014, 136, 8368−8373

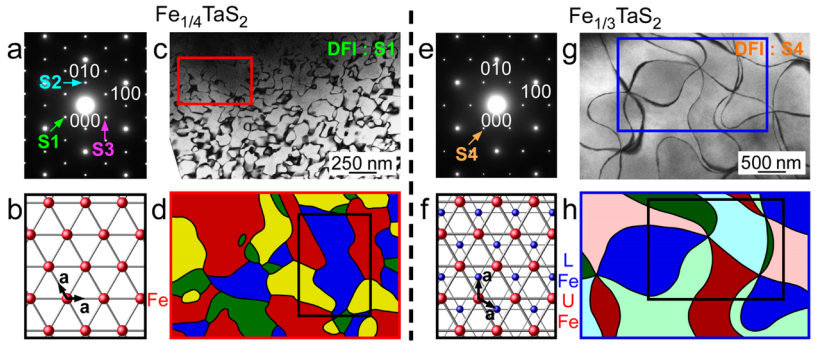

Figure 1. Electron diffraction patterns and domain structures of $Fe_{1/4}TaS_2$ and $Fe_{1/3}TaS_2$. (a,e) Electron diffraction patterns of Fe_xTaS_2 with $x \approx 1/4$ and 1/3, respectively. The 2a × 2a-type (indicated by S1, S2 and S3) and $\sqrt{3}$a × $\sqrt{3}$a-type (indicated by S4) superlattice spots can be observed clearly in addition to the fundamental spots. Note that the electron incidence is almost parallel to the [001] direction. (b,f) Two-dimensional schematics of the 2a × 2a and $\sqrt{3}$a × $\sqrt{3}$a superstructures of intercalated Fe ions in $Fe_{1/4}TaS_2$ and $Fe_{1/3}TaS_2$, respectively. The red and blue spheres depict Fe ions, and small (large) spheres represent the lower (upper) Fe layers. (c,g) Dark-field images taken using the superlattice spots indicated by S1 and S4, respectively. Note that some antiphase boundaries are invisible in (c) because of the extinction rule. (d,h) Domain patterns with four proper coloring (red, yellow, blue, and green) in $Fe_{1/4}TaS_2$ and tensorial proper coloring (first step = dark and light; second step = red, blue, and green) in $Fe_{1/3}TaS_2$, respectively. The (d) and (h) schematics correspond to the red- and blue-framed areas in (c) and (g), respectively.

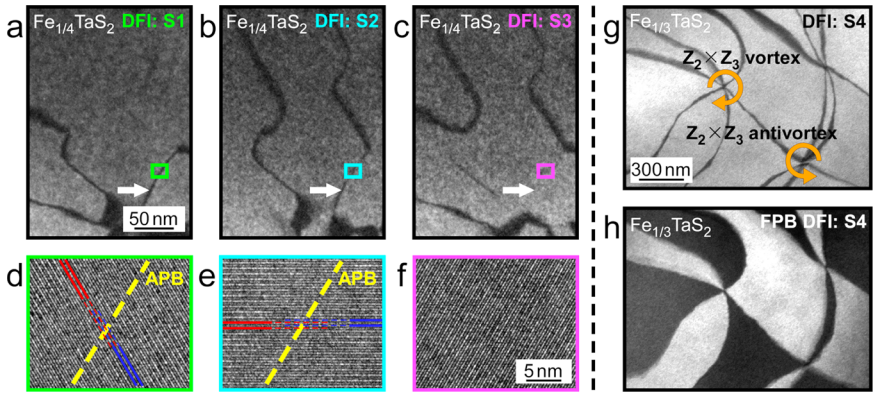

Figure 2. Antiphase and chiral domains in Fe_xTaS_2. (a–c) Dark-field images of $Fe_{0.25}TaS_2$ taken using superlattice spots indicated by S1, S2, and S3 in Figure 1a, respectively. These images correspond to the black-box area in Figure 1d. (d–f) High-resolution TEM images from the color-box areas in (a), (b), and (c), respectively. The antiphase boundary is indicated with a dashed yellow line. (g,h) Dark-field images of $Fe_{0.43}TaS_2$ taken using the superlattice spot indicated by S4 in Figure 1e. The dark-field image in (h) taken under the so-called Friedel's-pair-breaking condition clearly exhibits the presence of chiral domains without centrosymmetry.

patterns and physical properties of Fe_xTaS_2 resembles the relation between the order without periodicity in the Fibonacci sequence, Penrose tiling, and the formation of quasicrystals;[24−26] it is also similar to the way that self-similarity plays the key role in the formation of fractals and dendrites.[27] Our discovery unveils the importance of understanding the global topology of domain configurations in functional materials.

■. EXPERIMENTAL SECTION

Thin plate-like single crystals of Fe_xTaS_2 were grown by a chemical vapor transport method.[19,20,28] Magnetic hysteresis curves of the crystals were obtained using a Quantum Design Magnetic Property Measurement System and the real Fe compositions were estimated from the saturation magnetic moments in the magnetic hysteresis curves with the assumption that each mole of Fe^{2+} ions exhibits the full moment of 4 μ_B/mol. The estimated Fe compositions of crystals with nominal compositions of 0.33, 0.4, 0.5, 0.6, and 0.7 are 0.18, 0.25, 0.34, 0.43, and 0.47, respectively. The estimated concentrations were used for the x values in this paper, and the samples with x = 0.25, 0.34, 0.43, and 0.47 were used for transmission electron microscopy (TEM) studies to investigate the superlattice domain structures. Specimens for TEM studies were prepared by mechanical cleaving, followed by Ar ion milling. TEM studies were carried out using JEOL-2010F and JEOL-2000FX microscopes at room temperature. The electron diffraction patterns and real-space images were recorded with a 14-bit charge-coupled-device array detector and imaging plates. The reflection spots in the diffraction patterns were indexed using a simple hexagonal notation.

■. RESULTS

The results of our TEM experiments reveal that in single-crystalline Fe_xTaS_2, $Fe_{0.25}$ shows 2a × 2a-type superlattice reflections, whereas $Fe_{0.34}$, $Fe_{0.43}$, and $Fe_{0.47}$ exhibit the $\sqrt{3}$a × $\sqrt{3}$a type, indicating that the change in the superstructure occurs somewhere between x = 1/4 and 1/3. Figure 1a and e display electron diffraction patterns of $Fe_{0.25}$ and $Fe_{0.43}$, respectively. The superlattice reflection spots are observed at the (1/2 0 0)-type and (1/3 1/3 0)-type reciprocal positions in $Fe_{0.25}$ and $Fe_{0.43}$, indicating the presence of 2a × 2a and $\sqrt{3}$a × $\sqrt{3}$a-type superstructures, respectively. Note that the intercalated Fe ions form a two-dimensional (2D) supercell between two adjacent Ta−S_6 prismatic layers (Supporting Information,

dx.doi.org/10.1021/ja5026134 | J. Am. Chem. Soc. 2014, 136, 8368−8373

section S1). The distinct feature between the 2a × 2a and $\sqrt{3}$a × $\sqrt{3}$a superstructures in Fe_xTaS_2 is the different stacking sequence of the 2D supercells along the *c* axis. Specifically, the 2a × 2a superstructure consists of identically stacked 2D supercells (i.e., AA-type stacking), whereas the $\sqrt{3}$a × $\sqrt{3}$a superstructure contains shifted 2D supercells with AB-type stacking, as shown in Figure 1b and f, respectively. These different stacking sequences result in the centrosymmetric $P6_3/mmc$ and noncentrosymmetric and chiral $P6_322$ space groups for the 2a × 2a and $\sqrt{3}$a × $\sqrt{3}$a superstructures, respectively.

We found complicated configurations of antiphase domains in the dark-field images of $Fe_{0.25}$ and $Fe_{0.43}$ taken using superlattice spots. The antiphase domain patterns of two specimens exhibit distinct features, even though their diffraction patterns appear similar, only differing in the exact position of the superlattice spots. For example, the antiphase domains in $Fe_{0.25}$ are significantly smaller than those in $Fe_{0.43}$. Figures 1c and 1g show the dark-field images taken using the $(\bar{1}/2\ 0\ 0)$ superlattice spot indicated as S1 in Figure 1a and the $(\bar{1}/3\ \bar{1}/3\ 0)$ superlattice spot denoted as S4 in Figure 1e, respectively. The antiphase boundaries, separating neighboring antiphase domains, are clearly visible as dark line contrasts in superlattice dark-field images in both cases. (Supporting Information, section S2).

There is an extinction rule for the dark-field images of antiphase boundaries in the 2a × 2a superstructure. For example, the antiphase boundary between the BB-type and CC-type antiphase domains appears in the S1 = $(\bar{1}/2\ 00)$ (Figure 2a) and S2 = (0 1/2 0) (Figure 2b) dark-field images but disappears in the S3 = $(1/2\ \bar{1}/2\ 0)$ dark-field image of Figure 2c (see also Supporting Information, section S3). Each antiphase boundary becomes invisible in a dark-field image taken using one out of three superlattice spots (namely, S1, S2, or S3), when no antiphase shift at the boundary exists along a certain superlattice modulation wave vector. This absence of antiphase shifts at the antiphase boundary leads to the extinction rule for the antiphase boundaries in superlattice dark-field images. This rule is summarized in Figure 3, showing the local structures near boundaries between two antiphase domains. The boundaries are highlighted with yellow bands, and the three directions of the superlattice modulation wave vectors are denoted by S1, S2, and S3, respectively, as shown in Figure 1a. The red, yellow, blue, and green circles correspond to AA-, BB-, CC-, and DD-type superstructures, respectively, which are associated with four possible origins of the 2a × 2a Fe superstructure. It is evident that the superlattice modulation along only one out of three equivalent crystallographic directions does not show any antiphase shift; this is indicated by light green arrow (along the S1 direction), light blue arrow (along the S2 direction), and pink arrow (along the S3 direction). For example, the antiphase boundary between BB-type and CC-type (or AA-type and DD-type) antiphase domains has antiphase shifts along the S1 and S2 directions, whereas no antiphase shift along the S3 direction. In other words, when a boundary along a BB-type (AA-type) antiphase domain disappears in a S3 superlattice dark-field image, the neighboring domain should be CC-type (DD-type). This extinction rule of antiphase boundaries allows us to identify four different antiphase domains in any complicated domain patterns. Furthermore, the exact nature of the antiphase boundaries in the boxed area in Figure 2a–c is unveiled in high-resolution TEM images (Figure 2d–f), showing the lattice fringes of superlattice modulations. The specimen was tilted

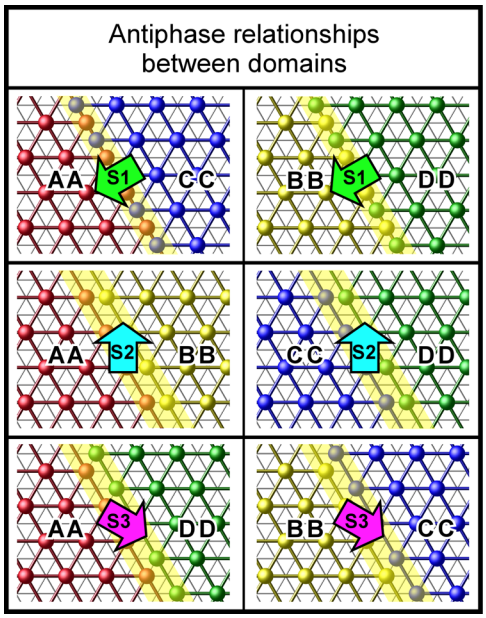

Figure 3. Extinction rule and local structure of antiphase boundaries in $Fe_{1/4}TaS_2$. The red, yellow, blue, and green circles correspond to AA-, BB-, CC-, and DD-type superstructures, respectively. The boundaries are highlighted with yellow bands. The superlattice modulation along one out of three equivalent crystallographic directions (S1 direction: light green arrow, S2 direction: light blue arrow, and S3 direction: pink arrow) does not show any antiphase shift, resulting in the absence of the antiphase boundary contrast in the corresponding superlattice dark-field image.

along the 100-type reciprocal axes to excite the superlattice reflection spots for Figure 2a–c, so the lattice fringes are perpendicular to the superlattice modulation wave vectors $\vec{q}$. The high-resolution TEM images clearly demonstrate that antiphase shifts appear only in Figure 2d and e, but there exists no antiphase shift in Figure 2f, indicating that this extinction rule originates from the local structure near the antiphase boundary (Supporting Information, section S4).

This extinction rule for the antiphase boundaries allows us to identify the four different antiphase domains in a complicated 2a × 2a superstructure domain configuration. A complete map of antiphase boundaries and domains obtained from all three distinct dark-field images (taken using three different superlattice spots, i.e., S1, S2, and S3) for the area in the red box in Figure 1c is shown in Figure 1d. We found that the complex antiphase domain pattern of the 2a × 2a superstructure in Figure 1c can be neatly understood in terms of the four color theorem. Mathematically, the four color theorem is stated as "all faces of every planar graph can be four-proper-colorable or Z_4-colorable". Consistent with this four color theorem, the pattern in Figure 1d for the 2a × 2a superstructure is Z_4 (red, blue, yellow, and green)-colorable, and these Z_4 colors correspond to the AA-, BB-, CC-, and DD-type 2a × 2a superstructures, respectively. The physical meaning of this intriguing correspondence between the four color theorem and the pattern for the 2a × 2a superstructure can be interpreted as follows: (1) there exists no particular rule for the 2a × 2a superstructure domain pattern, (2) domain size tends to be small if there exists no rule for a global domain configuration, and (3) most importantly, all boundaries are coherent, and there exist no disordered (incoherent) boundaries in the 2a × 2a superstructure domain pattern.

dx.doi.org/10.1021/ja5026134 | J. Am. Chem. Soc. 2014, 136, 8368–8373

In contrast to that of the 2a × 2a superstructure, the domain configuration of the $\sqrt{3}a \times \sqrt{3}a$ superstructure exhibits a unique topology, and the domains tend to be significantly larger. First of all, the typical domain size in $Fe_{0.43}$ is about 3 μm, whereas that in $Fe_{0.25}$ is about 150 nm. Second, six antiphase boundaries of the $\sqrt{3}a \times \sqrt{3}a$ superstructure merge always at one point without any exception, and thus, the superstructure domain pattern forms a 6-valent graph. Furthermore, each domain is always surrounded by an even number of vertices, thus forming a so-called "even-gon". The concept of the standard one-step proper coloring can be extended to that of two-step (tensorial) proper coloring, and all faces of every 6-valent graph with even-gons are tensorial-$Z_2 \times Z_3$-colorable.[29] It turns out that all faces of every 6-valent graph with even-gons are two-proper-colorable. After this first-step two-proper coloring (with dark and light colors), faces with dark or light colors can be further colored with three colors (with red, blue, and green colors) in such a way that each face is surrounded neither by any face with the same "first" color nor by any face with the same "second" color. For example, a dark red face is never surrounded by any light red face or any dark faces. This nontrivial process turns out to be unique. This $Z_2 \times Z_3$-coloring for the area in the blue box in Figure 1g is displayed in Figure 1h (see also Supporting Information, section S5).

The Z_4-coloring and $Z_2 \times Z_3$ tensorial coloring in $Fe_{0.25}$ and $Fe_{0.43}$, respectively, is summarized in Figure 4. Figure 4a shows

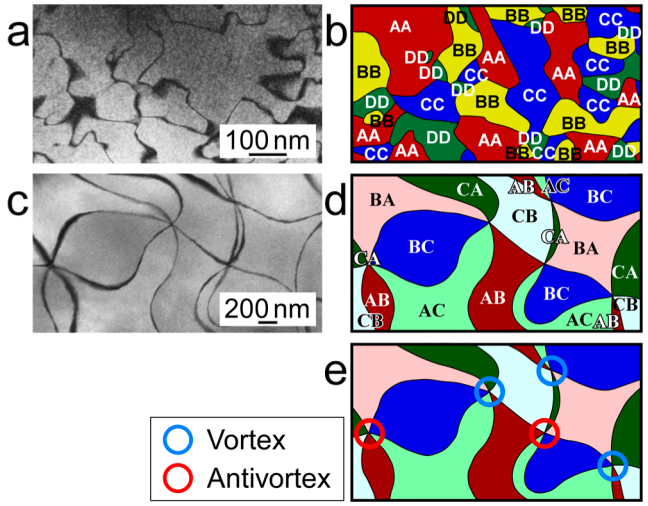

Figure 4. Antiphase domains in Fe_xTaS_2 and proper coloring of them. (a) Superlattice dark-field image of $Fe_{0.25}$ from the red-framed area in Figure 1c. Note that some antiphase boundaries are invisible because of the extinction rule. (b) A complete antiphase domain pattern of $Fe_{0.25}$ with Z_4 coloring. All antiphase domains were identified using the extinction rule and are consistent with the Z_4 colors. (c) superlattice dark-field image of $Fe_{0.43}$ from the blue-framed area in Figure 1g. (d) An antiphase and chiral domain pattern of $Fe_{0.43}$ with $Z_2 \times Z_3$ coloring. (e) $Z_2 \times Z_3$ vortices and antivortices in the antiphase and chiral domain pattern. The vortices and antivortices are indicated by blue and red circles, respectively.

the superlattice dark-field image of $Fe_{0.25}$ from the red-framed area in Figure 1c. The antiphase domain boundaries can be observed as dark lines. A complete antiphase domain pattern of $Fe_{0.25}$ with Z_4 coloring is depicted in Figure 4b. Note that the domain pattern is obtained from superlattice dark-field images taken using various superlattice spots. All antiphase domains were identified using the extinction rule and are denoted AA, BB, CC, and DD; these four types of antiphase domains are represented by Z_4 colors (red, blue, green, and yellow). Figure 4c and d show the superlattice dark-field image of $Fe_{0.43}$ (from the blue-framed area in Figure 1g) and an antiphase and chiral domain pattern of $Fe_{0.43}$ with $Z_2 \times Z_3$ coloring. The $Z_2 \times Z_3$ colors have one-to-one correspondence with chiral and antiphase domains; in other words, Z_2 corresponds to two types of chirality, and Z_3 represents three antiphase domains.

The $Z_2 \times Z_3$ coloring for the $\sqrt{3}a \times \sqrt{3}a$ superstructure domains is associated with profound physical consequences. First, Z_3 (red, blue, and green) colors correspond to three types of $\sqrt{3}a \times \sqrt{3}a$ superstructure antiphase domains, that is, AB-, BC-, and CA-type antiphase domains. The Z_2 coloring is associated with chiral domains without centrosymmetry. These chiral domains are clearly observed in the dark-field image taken using the S4 = $(\bar{1}/3\ \bar{1}/3\ 0)$ superlattice spot under the so-called Friedel's-Pair-Breaking condition,[30] as shown in Figure 2h. On the other hand, the dark-field image in Figure 2g, taken using the same S4 superlattice spot with the electron incidence almost parallel to the [001] zone axis, shows only antiphase boundaries. The top-view and side-view stacking structures of the 2D Fe supercells in $x \approx 1/4$ (AA-type) and in $x \approx 1/3$ (AB-type) are depicted in Figure 5a and b, respectively. Inversion symmetry is broken in $x \approx 1/3$ because the inversion center of the TaS_2 lattice along the c axis does not match with that of the Fe lattice with the AB-type stacking, whereas inversion symmetry remains intact in $x \approx 1/4$ with the AA-type stacking. Intercalation of Fe ions tends to induce rotation of Ta−S_6 prisms around Fe ions in $x \approx 1/3$, and the opposite rotation of the top and bottom Ta−S_6 prisms around each intercalated Fe ion induces chirality in $x \approx 1/3$ with the AB-type stacking (Supporting Information, section S1 and S6).

■. DISCUSSION

The diffusion of intercalated Fe ions is expected to be important for the formation of the complex domains in Fe_xTaS_2, and the stacking of 2D supercells (AA-type in $x \approx 1/4$ or AB-type in $x \approx 1/3$) may play a key role in forming the Z_4 or $Z_2 \times Z_3$ domain patterns. In $x \approx 1/4$, the intercalated Fe ions sit at the same position along the c axis and the Ta ions in between are therefore not distorted (Figure 5a). As a result, four types of antiphase domains related to the presence of four Fe positions (i.e., AA-, BB-, CC-, and DD-type) can form during the disorder−order transition of Fe ions, resulting in the Z_4 domain pattern where the antiphase domains are distributed without any regularity. On the other hand, in $x \approx 1/3$, the intercalated Fe ions on the upper and lower Fe layers are shifted and Ta ions can therefore distort along the c axis (Figure 5b). These Ta distortions can induce intriguing energetics in such a way that, for example, near the boundary region between A- and B-type 2D supercells within one layer, a C-type supercell is stable in the next layer, which leads to the two adjacent AC- and BC-type domains (Supporting Information, section S4). A topological defect structure with six BC/AC/AB/CB/CA/BA domains (in a counterclockwise direction) can be realized through this process, as shown in Figure 5c. Note that (1) when cyclicity and chirality is considered, BC/AC/AB/CB/CA/BA domains can be renamed A+/B−/C+/A−/B+/C− domains, respectively (Supporting Information, section S7), (2) a vorticity can be defined for a topological defect with A+/B−/C+/A−/B+/C− domains, so the defect can be considered a topological vortex with $Z_2 \times Z_3$ patterns, that is, a $Z_2 \times Z_3$ vortex, and (3) an adjacent

dx.doi.org/10.1021/ja5026134 | J. Am. Chem. Soc. 2014, 136, 8368−8373

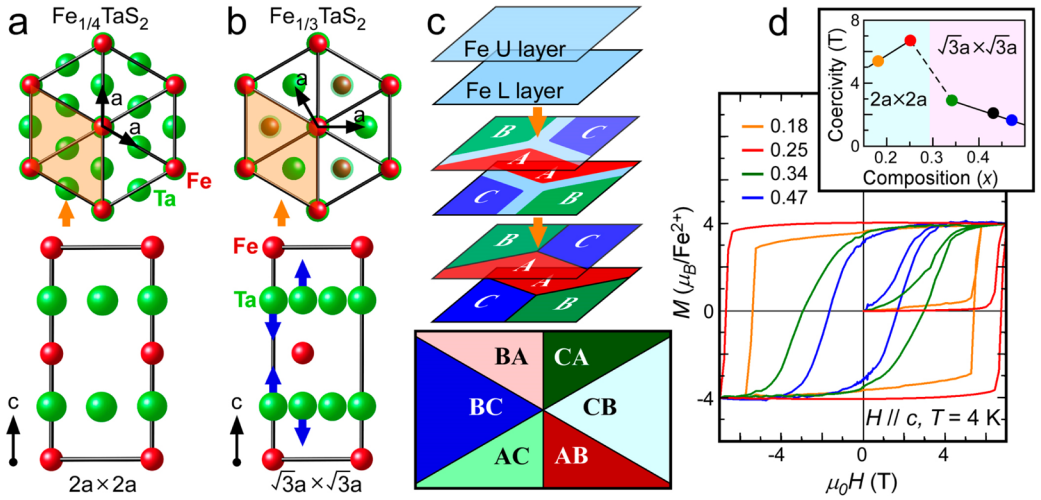

Figure 5. Domain evolution and magnetic properties in Fe_xTaS_2. (a,b) The top-view and side-view schematics of the crystallographic structures of $Fe_{1/4}TaS_2$ and $Fe_{1/3}TaS_2$, respectively. Only Fe (red) and Ta (green) ions are depicted. The side-view schematics correspond to the portions indicated in orange in the top-view schematics. The arrows depict the displacement of Ta ions along the *c* axis. (c) Schematics of the evolution of a $Z_2 \times Z_3$ domain during the disorder−order transition of Fe ions. (d) Magnetic hysteresis curves of $x = 0.18$, 0.25, 0.34, and 0.47. These curves were measured at 4 K in magnetic fields along the *c* axis. Note that $x = 0.18$ and 0.25 show the 2a × 2a-type superstructure, whereas $x = 0.34$ and 0.47 exhibit the $\sqrt{3}a \times \sqrt{3}a$-type one. The inset shows the magnetic coercivity as a function of Fe composition.

topological defect with A+/C−/B+/A−/C+/B− has the opposite vorticity, so it can be considered a topological antivortex. Vortices (blue circles) and antivortices (red circles) associated with the antiphase and chiral domains are identified in Figure 4e. It is evident that a vortex is surrounded by antivortices and vice versa.

We found that the domain topology in Fe_xTaS_2 has a significant effect on the magnetic properties. Figure 5d shows magnetic hysteresis (M(H)) curves measured at 4 K with the magnetic field parallel to the *c* axis, and magnetic coercivity, extracted from M(H) curves, vs *x* in Fe_xTaS_2. The M(H) curves of $Fe_{0.18}$ and $Fe_{0.25}$, showing Z_4 domain patterns with small domain sizes, exhibit sharp switching of magnetization with large coercivities. On the other hand, the M(H) curves of $Fe_{0.34}$ and $Fe_{0.47}$ with $Z_2 \times Z_3$ domain patterns with large domain sizes show relatively broad switching of magnetization with small coercivity (Supporting Information, section S8). High-density antiphase boundaries associated with Z_4 domains are probably associated with a strong pinning effect of magnetic domain walls and lead to an avalanche-like depinning of magnetic domain walls in the presence of high external magnetic fields.[19,20] On the other hand, large $Z_2 \times Z_3$ domains with a small number of antiphase/chiral domain boundaries accompany weak pinning of magnetic domain walls and a small coercivity field.

In summary, Fe ionic ordering in Fe_xTaS_2 induces two types of superstructures: centrosymmetric 2a × 2a and chiral $\sqrt{3}a \times \sqrt{3}a$ types. The topologies of the complex antiphase domains of these 2a × 2a and $\sqrt{3}a \times \sqrt{3}a$ superstructures are associated with Z_4 and $Z_2 \times Z_3$ coloring, respectively. We also found that these different topologies have significant physical consequences, such as domain size and magnetic properties. Our findings provide new insights for understanding and controlling domains in complex functional materials.

■ ASSOCIATED CONTENT

Ⓢ Supporting Information

Additional information on crystal structures, antiphase domain boundaries, extinction rule at antiphase domain boundaries and identification of antiphase domains, local structures at antiphase domain boundaries, $Z_2 \times Z_3$ coloring of large-range antiphase domain image, chirality, local distortions near a vortex core, and difference of Z_4 and $Z_2 \times Z_3$ antiphase domains in size. This material is available free of charge via the Internet at http://pubs.acs.org.

■ AUTHOR INFORMATION

Corresponding Author

sangc@physics.rutgers.edu

Present Addresses

¶Department of Materials Sciences and Engineering, Kyushu Institute of Technology, Fukuoka 804-8550, Japan

△Advancement for College Education Center, Konyang University, Chungnam 320-711, Korea.

Notes

The authors declare no competing financial interests.

■ ACKNOWLEDGMENTS

We would like to thank Y. J. Choi and Weida Wu (Rutgers) for useful discussion. This work was supported by the NSF under Grant No. NSF-DMREF-1104484. The work at Postech was supported by the Max Planck POSTECH/KOREA Research Initiative Program [Grant No. 2011-0031558] through NRF of Korea funded by MEST.

■ REFERENCES

(1) Hubert, A.; Schafer, R. *Magnetic domains*; Springer: Berlin Heidelberg, 1998.

(2) Strukov, B. A.; Levanyuk, A. P. *Ferroelectric Phenomena in Crystals*; Springer: Berlin Heidelberg, 1998.

(3) Salje, E. K. H. *Phase transitions in ferroelastic and co-elastic crystals*; Cambridge Univ. Press: Cambridge, 1990.

(4) Sapriel, J. *Phys. Rev. B: Solid State* **1975**, *12*, 5128−5140.

(5) Schopohl, N.; Sluckin, T. J. *Phys. Rev. Lett.* **1988**, *60*, 755−755.

(6) Wilson, J. A.; DiSalvo, F. J.; Mahajan, S. *Adv. Phys.* **1975**, *24*, 117−201.

(7) Morris, R. C.; Coleman, R. V.; Bhandari, R. *Phys. Rev. B: Solid State* **1972**, *5*, 895−901.

(8) Nagata, S.; Aochi, T.; Abe, T.; Ebisu, S.; Hagino, T.; Seki, Y.; Tsutsumi, K. *J. Phys. Chem. Solids* **1992**, *53*, 1259−1263.
(9) Kumakura, T.; Tan, H.; Handa, T.; Morishita, M.; Fukuyama, H. *Czech. J. Phys.* **1996**, *46*, 2611−2612.
(10) Moncton, D. E.; Axe, J. D.; DiSalvo, F. J. *Phys. Rev. B: Solid State* **1977**, *16*, 801−819.
(11) Suits, B. H.; Couturie, S.; Slichter, C. P. *Phys. Rev. Lett.* **1980**, *45*, 194−197.
(12) Suits, B. H.; Couturie, S.; Slichter, C. P. *Phys. Rev. B: Condens. Matter Mater. Phys.* **1981**, *23*, 5142−5151.
(13) Chen, C. H.; Gibson, J. M.; Fleming, R. M. *Phys. Rev. Lett.* **1981**, *47*, 723−725.
(14) Chen, C. H.; Gibson, J. M.; Fleming, R. M. *Phys. Rev. B: Condens. Matter Mater. Phys.* **1982**, *26*, 184−205.
(15) Koyama, Y.; Zhang, Z. P.; Sato, H. *Phys. Rev. B: Condens. Matter Mater. Phys.* **1987**, *36*, 3701−3711.
(16) Friend, R. H.; Beal, A. R.; Yoffe, A. D. *Philos. Mag.* **1977**, *35*, 1269−1287.
(17) Parkin, S. S. P.; Friend, R. H. *Philos. Mag. B* **1980**, *41*, 65−93.
(18) Parkin, S. S. P.; Friend, R. H. *Philos. Mag. B* **1980**, *41*, 95−112.
(19) Morosan, E.; Zandberge, H. W.; Dennis, B. S.; Bos, J. W. G.; Onose, Y.; Klimczuk, T.; Ramirez, A. P.; Ong, N. P.; Cava, R. J. *Phys. Rev. B: Condens. Matter Mater. Phys.* **2007**, *75*, 104401.
(20) Choi, Y. J.; Kim, S. B.; Asada, T.; Park, S.; Wu, Weida; Horibe, Y.; Cheong, S.-W. *Euro. Phys. Lett.* **2009**, *86*, 37012.
(21) Appel, K.; Haken, W. *Am. Math. Soc. Bull.* **1976**, *82*, 711−712.
(22) Appel, K.; Haken, W. *Illinois J. Math.* **1977**, *21*, 429−490.
(23) Appel, K.; Haken, W.; Koch, J. *Illinois J. Math.* **1977**, *21*, 491−567.
(24) Shechtman, D.; Blech, I.; Gratias, D.; Cahn, J. W. *Phys. Rev. Lett.* **1984**, *53*, 1951−1953.
(25) Levine, D.; Steinhardt, P. J. *Phys. Rev. Lett.* **1984**, *53*, 2477−2480.
(26) Levine, D.; Steinhardt, P. J. *Phys. Rev. B: Condens. Matter Mater. Phys.* **1986**, *34*, 596−616.
(27) Sander, L. M. *Nature* **1986**, *322*, 789−793.
(28) Eibschutz, M.; Mahajan, S.; DiSalvo, F. J.; Hull, G. W.; Waszczak, J. V. *J. Appl. Phys.* **1981**, *52*, 2098−2100.
(29) Chae, S. C.; Horibe, Y.; Jeong, D. Y.; Lee, N.; Iida, K.; Tanimura, M.; Cheong, S.-W. *Phys. Rev. Lett.* **2013**, *110*, 167601.
(30) Tanaka, M.; Honjo, G. *J. Phys. Soc. Jpn.* **1964**, *19*, 954−970.